PCCP

PAPER

View Article Online
View Journal | View Issue

Cite this: *Phys. Chem. Chem. Phys.*, 2014, **16**, 15444

The surface chemistry of NO_x on mackinawite (FeS) surfaces: a DFT-D2 study

N. Y. Dzade, A. Roldan and N. H. de Leeuw*

Received 17th March 2014,
Accepted 4th June 2014

DOI: 10.1039/c4cp01138d

www.rsc.org/pccp

We present density functional theory calculations with a correction for the long-range interactions (DFT-D2) of the bulk and surfaces of mackinawite (FeS), and subsequent adsorption and dissociation of NO_x gases (nitrogen monoxide (NO) and nitrogen dioxide (NO_2)). Our results show that these environmentally important molecules interact very weakly with the energetically most stable (001) surface, but adsorb relatively strongly onto the FeS(011), (100) and (111) surfaces, preferentially at Fe sites *via* charge donation from these surface species. The NO_x species exhibit a variety of adsorption geometries, with the most favourable for NO being the monodentate Fe–NO configuration, whereas NO_2 is calculated to form a bidentate Fe–NOO–Fe configuration. From our calculated thermochemical energy and activation energy barriers for the direct dissociation of NO and NO_2 on the FeS surfaces, we show that NO prefers molecular adsorption, while dissociative adsorption, *i.e.* NO_2 (ads) → [NO(ads) + O(ads)] is preferred over molecular adsorption for NO_2 onto the mackinawite surfaces. However, the calculated high activation barriers for the further dissociation of the second N–O bond to produce either [N(ads) and 2O(ads)] or [N(ads) and O_2(ads)] suggest that complete dissociation of NO_2 is unlikely to occur on the mackinawite surfaces.

1. Introduction

The removal of nitrogen oxides (NO_x) from lean exhaust streams remains one of the major challenges in environmental catalysis and a topic of extensive research.[1–7] Atmospheric nitrogen oxides play an important role in the formation of photochemical smog and acid rain and the destruction of ozone in the stratosphere, whereas it is also a possible greenhouse gas exacerbating climate change.[8] It is obviously important that the concentration of NO_x gases in the atmosphere is stabilized, but as the population has grown and industrial activities have increased, the rate of NO_x emission from automobile exhausts and stationary sources has also increased dramatically over the years. In order to abate NO_x released into the environment, there is a need to develop novel catalysts with high efficiency towards the removal or destruction of NO_x (deNO_x processes). The adsorption and activation processes of NO_x over the active sites of a catalyst are a crucial part of the selective catalytic reduction (SCR) reactions of nitrogen oxides.[9]

Earlier investigations have focused on the adsorption of NO_x onto transition metal oxides *e.g.* TiO_2, BaO, ZnO and Al_2O_3 surfaces.[6,10–13] The adsorption and decomposition of NO_2 have also been investigated extensively using techniques such as temperature programmed desorption (TPD), low-energy electron diffraction (LEED), electron energy loss spectroscopy (EELS) and X-ray photoelectron spectroscopy (XPS) on pure metallic surfaces, such as, Pt(111),[14–17] Ru(001),[18,19] Rh(111),[20] Ag(111),[21–24] Pd(111),[25,26] Au(111),[27–30] and polycrystalline Au.[31] These studies have demonstrated that NO_2 adsorbs dissociatively onto Rh(111), Pd(111), Pt(111), Ru(001), and Ag(111) surfaces at low temperature but adsorbs molecularly onto Au(111) and polycrystalline Au.

Transition metal (TM) sulfide nanocrystals are attracting attention for potential applications in heterogeneous catalysis, solar cells, and light-emitting diodes owing to their unique and interesting physical, electronic, magnetic and chemical properties.[32–40] Iron sulfides are suggested catalysts in the iron-sulfur hypothesis for the origin of life. Pioneering research into evolutionary biochemistry by Wächtershäuser and others has suggested that many of the prebiotic chemical reactions might be catalysed by iron sulfide (mackinawite, greigite, pyrite and violarite) surfaces at hydrothermal vents on the ocean floor during the Hadean and early Archean eras.[41–43] Nørskov and co-workers have also reported the extraordinary catalytic properties of MoS_2 surfaces and MoS nanoparticles.[44,45] For example, in petrochemical processes, sulfur-containing molecules are removed from the feedstream by adsorption onto TM-sulfides, mainly MoS_2.[45–48] Recently, the interaction of NO_x with the (100) pyrite (FeS_2) surface has been reported by Sacchi *et al* using electronic structure calculations based on DFT.[49] The NO_x species were shown to interact strongly with the FeS_2(100) surface but the calculated high activation barriers for their dissociation suggest that the NO_x

Department of Chemistry, University College London, 20 Gordon Street, London, WC1H 0AJ, UK. E-mail: nelson.dzade.10@ucl.ac.uk, n.h.deleeuw@ucl.ac.uk

species will remain molecularly chemisorbed on pyrite surfaces even at high temperature. However, the diversity of naturally occurring iron sulfides, with iron existing in multiple oxidation states provides alternative iron sulfide systems for consideration as materials for the adsorption and decomposition of NO_x.

In this study, we have investigated the catalytic properties of mackinawite (tetragonal FeS) towards NO_x adsorption and activation using DFT calculations, where we consider the nature of binding of the NO_x species to the FeS surfaces and their dissociation reaction mechanisms. Mackinawite (FeS) is the first crystalline iron sulfide phase that is formed in aqueous systems and it is a precursor to the formation of sedimentary pyrite (FeS_2) and greigite (Fe_3S_4).[50,51] Earlier studies have demonstrated that mackinawite can influence the mobility and bioavailability of environmentally important trace elements, notably through processes involving either sorption[52,53] or oxidative dissolution.[54–56] A wealth of information is available in the literature regarding its bulk properties, such as the unit cell parameters, and the electronic, magnetic and mechanical properties of mackinawite.[57–62] The gradual oxidation processes of mackinawite have also been studied using X-ray diffraction (XRD), transition electron microscopy (TEM), transition Mössbauer spectroscopy (TMS) and X-ray photoelectron spectroscopy (XPS).[63]

Surprisingly, the chemical activity of mackinawite and in particular, its potential for catalytic applications has not been thoroughly investigated. In an earlier study, we have investigated the adsorption and desorption properties of the methylamine capping agent on various low-Miller index surfaces of FeS.[38] The present study, however, is aimed at providing a general understanding of FeS–NO_x interactions to assess mackinawite's potential as a nanocatalyst for the adsorption, activation and decomposition of environmentally important NO_x gases.

2. Computational methods

All calculations were performed using the Vienna Ab-initio Simulation Package (VASP) within the Kohn–Sham (KS) implementation of density functional theory (DFT) using plane-wave basis sets.[64–67] Dispersion forces were accounted for in our calculations using the Grimme DFT-D2 method[68] which is essential for an appropriate description of mackinawite.[38] We have used the generalized gradient approximation (GGA), with a density functional built from the Perdew and Zunger[69] local functional, and the gradient corrections by Perdew *et al.*[70] The interaction between the valence electrons and the core was described using the projected augmented wave (PAW) method[71] in the implementation of Kresse and Joubert.[72] The KS valence states were expanded in a plane-wave basis set with a cut off at 400 eV, which is high enough to ensure that no Pulay stresses occurred within the cell during relaxation. An energy threshold defining self-consistency of the electron density was set to 10^{-5} eV and the interatomic forces are minimized up to 0.01 eV $Å^{-1}$ for structural relaxation. For the geometry optimization calculations, 11 × 11 × 11 and 5 × 5 × 1 Monkhorst-pack grids were used to sample the reciprocal space of bulk FeS and the substrate–adsorbate system respectively, which ensures electronic and ionic convergence.

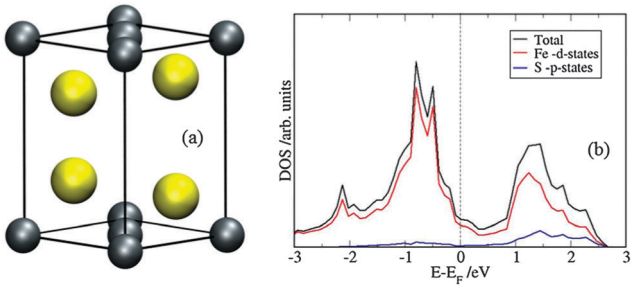

Fig. 1 The tetragonal FeS structure (a), and the electronic density of state of bulk mackinawite (b). (Colour scheme: Fe = grey and S = yellow).

The bulk FeS was modelled in the tetragonal structure (see Fig. 1a) in the non-magnetic state, reflecting the fact that both room temperature neutron diffraction[59] and Mössbauer data[60] at 4.2 K with an external field testify the absence of an iron magnetic moment in mackinawite. This effect has been attributed to strong covalency in the Fe–S bonding,[59] on the one hand and to extensive d-electron delocalisation within the sheets,[60] on the other hand. An earlier DFT structural optimization of FeS performed by Devey *et al.* also predicted the stable ground state to be nonmagnetic.[39] The different low-Miller index FeS surfaces were created from the optimized bulk using the METADISE code,[73] which not only considers the periodicity in the plane direction but also provides the different atomic layer stacking resulting in a zero dipole moment perpendicular to the surface plane, as is required for reliable and realistic surface calculations.[74] A vacuum region of 15 Å along the *c*-axis was tested to be sufficient to avoid interactions between the surface slab and its periodic image, and from our convergence of the number of FeS layers to represent the bulk, we identified that three FeS layers were sufficient to model the surfaces of mackinawite reliably. For the isolated NO_x species we have used a cell with lattice constants of 15 Å, sampling only the Γ-point of the Brillouin zone. To determine the optimum adsorption geometries, the atoms of the adsorbate and the topmost two FeS layers of the (4 × 2) slab were allowed to relax without constraints until the residual forces on each atom reached 0.01 eV $Å^{-1}$.

The Bader charge analysis was carried out for all the adsorbate–substrate systems, using the Henkelman algorithm[75,76] in order to quantify the charge transfer between the FeS surfaces and NO_x species. The nudged elastic band (NEB) method was used to locate the transition state and reaction activation energy barriers of the NO_x dissociation process.[77,78] Transition states were further confirmed through frequency calculations, in which only one imaginary frequency is obtained corresponding to the reaction coordinate. The reaction energy (ΔE) is calculated as the total energy difference between the final state and the initial state and the activation barrier (E_a) is defined as the total energy difference between the initial state and the saddle point.

3. Results and discussion

3.1 Bulk properties

Mackinawite crystallises in a tetragonal structure (Fig. 1) with space group *P*4/*nmm* (no. 129).[57,58] In the mackinawite structure, each iron atom is arranged in tetrahedral coordination with sulfur in a square lattice to form edge-sharing tetrahedral layered sheets stacked along the *c*-axis and stabilized *via* van der Waals forces.[79] Each iron atom is in square-planar coordination with neighbouring irons at a Fe–Fe distance of 2.597 Å,[57] which is similar to the Fe–Fe distance in bcc Fe (2.482 Å).[80] The interlayer separation distance (the *c*-parameter) and the unit cell edge length in the *a* and *b* directions are normally used to characterize the mackinawite cell. Using the theoretical method described above and allowing all atoms to fully relax until the required accuracy was reached, we calculated the unit cell parameters at $a = b = 3.587$ Å and $c = 4.908$ Å with c/a ratio = 1.368 Å, which compares well with the range of experimental values reported in Table 1.[51,57,58,81,82] Because mackinawite is easily oxidised, the lattice parameters of synthetic mackinawite are sensitive to the synthesis conditions and handling of the samples before characterization and it is clear from the range of lattice parameters in Table 1 that especially the interlayer separation (*c*-parameter) of synthetic mackinawite varies significantly between samples. The mackinawite samples characterized by Lennie *et al.*[57] were synthesized by reacting iron with Na_2S solutions, vacuum dried and sealed under vacuum in borosilicate glass tubes to prevent oxidation before analysis. The samples obtained were described to be well-crystalline mackinawite samples and therefore are highly suitable for comparison with theory. The much larger interlayer separation distance of the mackinawite characterized by Wolthers *et al.*[82] was attributed to both intercalation of water molecules between the layers of mackinawite and lattice relaxation with decreasing crystallite size.

The good agreement of the calculated lattice parameters with experiment is due to the inclusion of the dispersion interactions in the DFT calculation. In layered materials such as mackinawite, where the layers are stabilized by weak van der Waals interactions, standard DFT methods often overestimate the interlayer spacing. In an earlier study we have shown that standard DFT methods poorly predict the interlayer spacing of mackinawite at 5.484 Å, representing an overestimation of about 10%[38] relative to experimental data from Lennie *et al.*[57] In this study, by implementing the DFT-D2 method of Grimme to account for the weak dispersion forces we have predicted the interlayer separation distance at 4.908 Å, which is only 2% smaller than the experimental value of Lennie,[57] suggesting the importance of this correction to include dispersion forces in accurately predicting the interlayer separation distance in mackinawite. Our calculated $a = b$ parameter of 3.587 Å is also within typical DFT errors (2%) of the experimental value of 3.674 Å.[57] In earlier theoretical calculations the interlayer separation distance was simply fixed at the experimental value of Lennie *et al.* (Devey *et al.*, 2008; Subedi *et al.*, 2008),[39,61] but this approach could introduce unrealistic strain in the surface calculations.

Our calculated electronic density of states (DOS) of bulk mackinawite (Fig. 1b) shows the Fermi energy cutting a band of the Fe d-orbital roughly in the centre of a local minimum, indicating a partial localization with regard to the S atoms but still metallic, in agreement with the metallic nature deduced by Vaughan and Ridout[60] and also consistent with earlier theoretical investigations.[39,61]

Table 1 Optimized structural parameters of FeS. The experimental unit cell parameters *a*, *b* and *c* and the *c*/*a* ratio are also given for comparison

Parameter	Experiment[51,57,58,81,82]	DFT-D2
$a = b$/Å	3.650–3.679	3.587
c/Å	4.997–5.480	4.908
c/a	1.363–1.501	1.368
d(Fe–S)/Å	2.240–2.256	2.262
d(Fe–Fe)/Å	2.598–2.630	2.536

3.2 Surface characterization

We have modelled the different low-Miller index surfaces by taking advantage of the crystal symmetry in the *a* and *b* directions to reduce the number of surfaces to the {001}, {100}, {011}, {110} and {111} family of surfaces. The {001} surface possesses two distinct terminations where the {001}-S surface corresponds to a termination of the complete FeS layer, leaving a typical type II-terminated[74] surface of S atoms (Fig. 2a), whereas the {001}-Fe surface is a reconstructed formally dipolar type III surface leaving a partially vacant layer of Fe atoms at the surface (Fig. 2b). The {100} surface possesses only a single repeat unit, but the {011}, {110}, and {111} surfaces also possess two possible terminations, a type II and a reconstructed type III. We have considered all the different possible terminations, but we have used only the most stable terminations to investigate the adsorption properties of NO_x. The surface energy of the relaxed surfaces was obtained using a combination of calculations for the relaxed and unrelaxed surfaces. After constructing the surface, and before optimization, the slab contains two unrelaxed surfaces and the unrelaxed surface energy (γ_u) may be obtained from a single point calculation as

$$\gamma_u = \frac{E_{slab}^{unrelaxed} - nE_{bulk}}{2A} \quad (1)$$

where $E_{slab}^{unrelaxed}$ is the energy of the unrelaxed slab, nE_{bulk} is the energy of an equal number (n) of bulk FeS units, and A is the area of one side of the slab. When only one side of the slab (top) is allowed to relax unconstrainedly, while the bottom layer atoms are fixed at the bulk parameters, as implemented in this

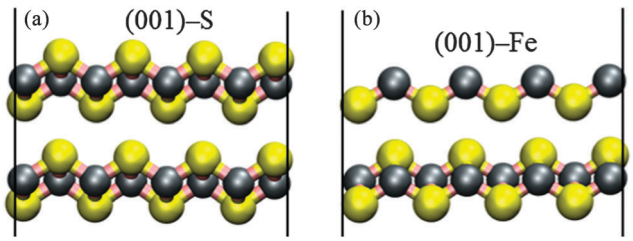

Fig. 2 Schematic of the sulfur terminated ((001)-S) and Fe terminated ((001)-Fe) surfaces of FeS(001). (Colour scheme: Fe = grey and S = yellow).

study, the additional energy due to the relaxed surface at the top of the slab must be separated from the energy of the unrelaxed surface at the bottom, as the two differ. From the unrelaxed surface energy it is possible to calculate the relaxed surface energy (γ_r) from the total energy of the relaxed slab as:

$$\gamma_r = \frac{E_{slab}^{relaxed} - nE_{bulk}}{A} - \gamma_u \quad (2)$$

where $E_{slab}^{unrelaxed}$ is the energy of the relaxed slab.

By substituting γ_u from eqn (1) into (2), the relaxed surface (γ_r) relation becomes:

$$\gamma_r = \frac{E_{slab}^{relaxed} - nE_{bulk}}{A} - \frac{E_{slab}^{unrelaxed} - nE_{bulk}}{2A} \quad (3)$$

The calculated relaxed surface energies of the different low-Miller index FeS surfaces are presented in Table 2. The most stable surface is calculated to be the {001}-S termination with a surface energy of 0.19 J m^{-2}, in agreement with an earlier interatomic potential study of mackinawite surfaces by Devey *et al.*[39] The creation of the {001}-S terminated surface involves only breaking of the weak vdW interactions between the sulfide layers which results in negligible relaxation of the surface species. The reconstructed {001}-Fe terminated surface, on the other hand, has a high surface energy (2.67 J m^{-2}) reflecting the fact that its creation requires breaking of the most Fe–S bonds. The surface energies of the most stable terminations of the {011}, {100}, {111} and {110} surfaces are calculated to be 0.95, 1.04, 1.51, and 1.72 J m^{-2} respectively. These surfaces are shown to undergo minimal relaxation as reflected in their topmost layer interatomic bond distances (Table 2) which are similar to those in the bulk. The relaxed structures of the energetically most stable terminations of the {011}, {100} and {111} surface slabs are shown in Fig. 3.

We have calculated the thermodynamic crystal morphology of mackinawite using Wulff's method,[83] which is based on the calculated surface energies. The calculated morphology of mackinawite (Fig. 4) shows excellent agreement with the crystals grown by Ohfuji and Rickard, who described thin and tabular crystals from their high resolution transmission electron microscope (HRTEM) examination of FeS aggregates.[84]

Table 2 Relaxed surface energies (γ) and the topmost layer internal bond distances for FeS

	(001)	(011)	(100)	(111)	(110)
γ/J m^{-2}	0.19	0.95	1.04	1.51	1.72
d(Fe–S)/Å	2.165	2.165	2.183	2.127	2.147
d(Fe–Fe)/Å	2.554	2.553	2.553	2.572	2.409

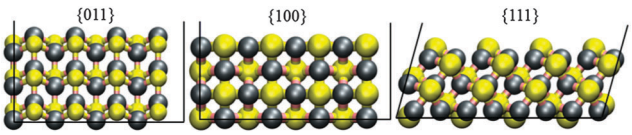

Fig. 3 Schematic of the most stable terminations of the {011}, {100} and {111} FeS surfaces. (Colour scheme: Fe = grey and S = yellow).

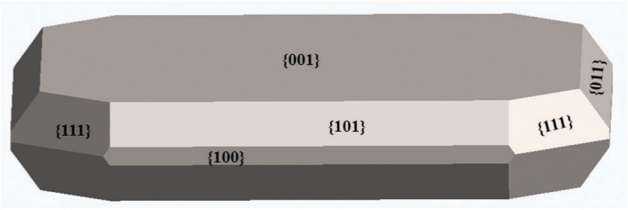

Fig. 4 Calculated crystal morphology of mackinawite. The crystals grow in tabular forms, with the {001} surface highly prominent.

Their complementary electron diffraction (SAED) analyses of selected areas of the FeS nanocrystals (both freeze-dried and precipitated mackinawite) show clearly {001} as the most stable surface, followed by the decreasing stabilities of the {101}, {200} (equivalent to the {100} surface), and {111} planes. These findings show good agreement with the surface energies predicted by our DFT calculations. The nonexistence of the {110} surface reflections in the SAED patterns and their lack of appearance in the calculated morphology of the FeS crystal can be attributed to its relatively high surface energy.

3.3 NO adsorption and dissociation

In order to identify the optimized adsorption structures with minimum energy on the {001}, {011}, {100} and {111} surfaces, we have placed the NO molecule on the surfaces in three different initial orientations: (1) oxygen pointing either towards (X–ON) or (2) away (X–NO) from the surface, and (3) NO adsorbed parallel to the surface plane (X–(NO)), where X denotes the interacting surface atom. To measure the strength of the adsorbate–surface interaction, we have calculated the adsorption energy (E_{ads}) using the relation in eqn (4).

$$E_{ads} = E_{surf+NO} - (E_{surf} + E_{NO}) \quad (4)$$

{001} surface. The adsorption of NO was first investigated on the most stable {001} surface where it was found to interact very weakly with the surface. The optimized low-energy NO adsorption structures on the {001} surface are shown in Fig. 5(a–c) while the adsorption energies and the relevant bond distances are summarized in Table 3. When adsorbed through its oxygen atom at the Fe site (Fig. 5a), the NO molecule was only physisorbed,

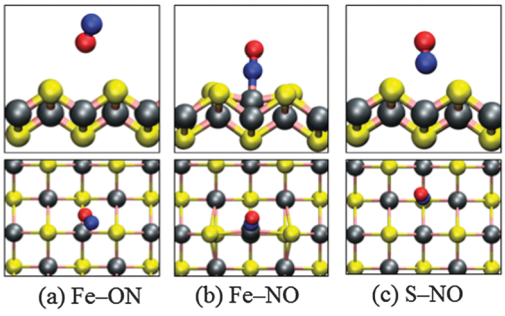

Fig. 5 Side (top) and top (bottom) views of the optimized adsorption structures of NO on the {001} FeS surface. (Colour scheme: Fe = grey, S = yellow, N = blue and O = red).

Table 3 Adsorption energies and the relevant bond distances of NO adsorbed onto the {001}, {011}, {100} and {111} FeS surfaces. $\sum q$ denotes the net charge gained by the NO molecule and υ(N–O) is the stretching vibrational frequency. The calculated free υ(N–O) = 1898 cm^{-1} and d(N–O) = 1.160 Å which compare well with the experimental[90] values of 1903 cm^{-1} and 1.170 Å, respectively

Surface	Configuration	E_{ads}/eV	d(Fe–N)/Å	d(Fe–O)/Å	d(N–O)/Å	υ(N–O)/cm^{-1}	$\sum q$/e$^-$
(001)	Fe–ON	−0.15	—	4.040	1.166	1845	0.00
	Fe–NO	+0.12	1.643	—	1.179	1793	0.06
	S–NO	−0.18	—	—	1.161	1839	0.00
(011)	Fe–NO	−2. 87	1.664	—	1.199	1766	0.45
	Fe–ON	−1.32	—	1.790	1.187	1616	0.39
	Fe–NO–Fe	−2.74	1.688	2.130	1.245	1375	0.70
(100)	Fe–NO	−2.91	1.656	—	1.197	1773	0.45
	Fe–ON	−1.33	—	1.792	1.186	1656	0.36
(111)	Fe–NO	−3.21	1.790	—	1.259	1575	0.64
	Fe–ON	−1.48	—	1.981	1.219	1568	0.45

releasing an adsorption energy of 0.22 eV, and it moved away from the surface Fe binding site during geometry optimization until the distance between the oxygen atom and the surface iron atom is 4.040 Å. When we adsorb NO *via* the nitrogen atom at the Fe site (Fe–NO), a positive adsorption energy of +0.12 eV was calculated, which suggests an unfavourable adsorption process. The Fe atom to which the NO is bound is pulled up by 1.201 Å from its surface position (see Fig. 5b), causing significant distortion of the surface structure around the Fe adsorption site, hence the unfavourable adsorption. The S–NO configurations (Fig. 5c) gave a very weak interaction; the NO molecule moved away from the interacting sulfur atom until the S–N distance is 3.068 Å, releasing an energy of 0.18 eV. The relaxed structure of the S–ON configuration converges to the Fe–ON configuration, giving the same binding energy (E_{ads} = 0.22 eV). As expected, no charge transfer occurred from the surface to the NO molecule except in the Fe–NO configuration where a small charge (0.06 e$^-$) is transferred from the surface. The calculated N–O stretching vibrational frequencies reported in Table 3 confirm no significant softening of the N–O bonds as they remained virtually unchanged compared to the isolated NO bond length. The weak interaction of the NO molecule with the {001} surface can be attributed to the steric repulsion the NO molecule experiences from the S atoms terminating the surface.

{011} surface. In contrast to the weak interaction with the {001} surface, the NO molecule adsorbs quite strongly at the {011} surface, preferentially at the top-Fe site; the sulfur sites are basically unreactive towards NO adsorption. The relaxed NO adsorption structures on the {011} surface are shown in Fig. 6(a–c). The lowest energy configuration was calculated to be the Fe–NO configuration (Fig. 6a), with the NO molecule binding perpendicularly to a top-Fe atom releasing an adsorption energy of 2.87 eV with the N–O and Fe–N bond distances calculated to be 1.199 Å and 1.664 Å respectively. The Fe–ON configuration (Fig. 6b) is found to be up to 1.55 eV less favourable, relative to the Fe–NO configuration, and its N–O and Fe–O bond distances are calculated to be 1.187 Å and 1.790 Å respectively. A stronger binding energy calculated for the Fe–NO configuration is similar to the results reported on the pyrite (100) surface, where the Fe–NO configuration was calculated

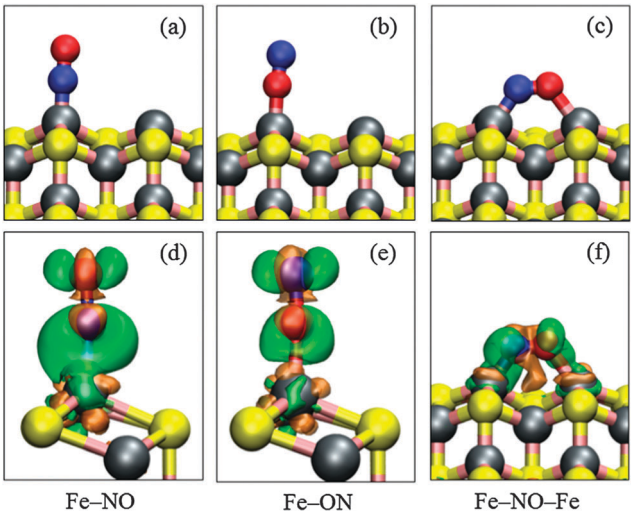

Fig. 6 Side views of the optimized adsorption structures of NO (a–c) on the {011} FeS surface. The corresponding electron density difference plots relative to the adsorbed NO, showing charge transfer in the regions between the NO and the surface Fe atoms upon adsorption, are displayed in (d–f). Green contours indicate electron density increase by 0.02 electrons per Å^3 and orange contours indicate electron density decrease by 0.02 electrons per Å^3. (Colour scheme: Fe = grey, S = yellow, N = blue and O = red).

to be 1.14 eV more favourable than the Fe–ON configuration.[49] Similarly, on transition metals, the M–NO configuration is often calculated to be energetically more favoured than the M–ON configuration.[85–87]

We have also identified a stable side-on configuration where the NO binds parallel at the bridge site between two adjacent Fe atoms on the {011} surface *via* the N and O atoms (denoted Fe–NO–Fe as shown in Fig. 6c). This configuration is found to be only 0.13 eV less favourable than the most stable Fe–NO configuration and the N–O, N–Fe and O–Fe bond distances are, respectively, calculated to be 1.245 Å, 1.688 Å and 2.130 Å. In Table 3, we present a summary of the adsorption energies and the relevant bond distances for NO adsorbed onto the {011} surface. The stretched N–O bonds, particularly in the side-on Fe–NO–Fe configuration, suggest that NO might dissociate

from this geometry but an attempt to cleave the N–O bond found this to be an overall endothermic process (ΔE = +0.60 eV) with an activation energy barrier of 1.16 eV. Another reaction path for NO dissociation was investigated, considering the most stable Fe–NO configuration as the starting point, but this reaction was also calculated to be endothermic (ΔE = +0.73 eV) overall and it has a very high activation energy barrier (4.12 eV), suggesting that NO will remain adsorbed molecularly onto the {011} surface. The transition state for the dissociation of NO from the Fe–NO configuration on the pyrite (100) surface was shown to possess a similarly high activation barrier of 5.44 eV.[49]

In agreement with the strong interaction of NO with the {011} surface, we show from our Bader population analysis that the NO molecule draws significant charge from the interacting surface Fe atoms upon adsorption, where in the Fe–NO, Fe–ON and Fe–NO–Fe configurations, the NO draws 0.45 e^-, 0.39 e^- and 0.70 e^-, respectively, which causes an elongation of the N–O bonds, as confirmed by the calculated N–O stretching vibrational frequencies presented in Table 3. Further insight into local charge rearrangement within the NO–surface system was gained from the electron density difference iso-surfaces, obtained by subtracting from the charge density of the total adsorbate system the sum of the charge densities of the molecule and the clean surface, calculated using the same geometry as the adsorbate system. In Fig. 6(d–f) we display the iso-surfaces of the electron density differences due to the adsorption of NO for the Fe–NO, Fe–ON, and Fe–NO–Fe configurations. From the charge density difference iso-surfaces, it is clear that electrons are depleted from Fe d-states and the NO internuclear axis region, but accumulate in the bonding region between NO and the surface Fe atoms, and on the NO molecule. The depletion of electron density from both the NO molecule and the surface Fe atoms shows that the interaction between NO and the surface corresponds to a donation and back-donation process,[88] wherein the NO donates electrons to the empty Fe d-orbitals and the filled Fe d-orbitals back-donate to the 2pπ* orbitals of NO. The net charge accumulated on the adsorbed NO molecule as calculated from the Bader population analysis discussed above, however, suggests a stronger back-donation from the filled Fe d-bands than the forward donation from the NO molecule.

{100} surface. The relaxed adsorption structures of NO on the {100} surface are shown in Fig. 7(a and b). No stable side-on configuration was found as the NO molecule flips back to the energetically most favoured Fe–NO configuration during geometry optimization. Similar to the {011} surface, the sulfur sites on the {100} surface remain unreactive towards NO adsorption compared to the Fe sites that are very reactive. The Fe–NO configuration (E_{ads} = −2.91 eV) is again calculated to be energetically more favourable than the Fe–ON configuration which releases an adsorption energy of 1.33 eV. In contrast to the perpendicularly adsorbed NO at the top-Fe sites on the {011} surface, the NO molecule is adsorbed in a tilted orientation onto the {100} surface with the N–O bond forming an angle of ∼60° and ∼41°, respectively, with the surface normal in the Fe–NO and Fe–ON configurations. Upon adsorption, the NO molecule draws charges of 0.45 e^- and 0.36 e^- from the {100} surface in

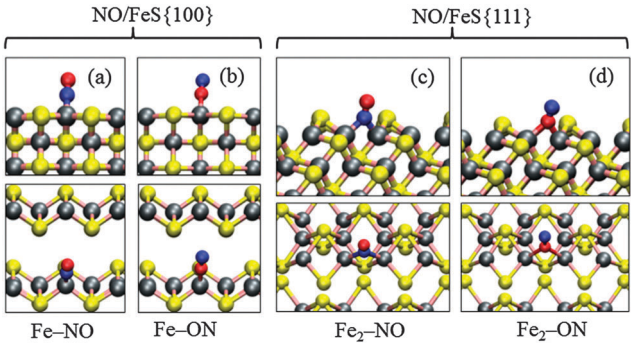

Fig. 7 Side and top views of the optimized adsorption structures of NO on the {100}-(a, b), and {111}-(c, d), FeS surfaces. (Colour scheme: Fe = grey, S = yellow, N = blue and O = red).

the Fe–NO and Fe–ON configurations, respectively, which causes an elongation of the N–O bonds calculated at 1.197 Å for the Fe–NO configuration and 1.186 Å for the Fe–ON configuration, compared with the free unperturbed bond length of 1.160 Å. All the relevant interatomic bond distances and the stretching N–O vibrational frequencies for NO adsorption onto the {100} surface are reported in Table 3. The dissociation of NO from the most stable Fe–NO configuration on the {100} surface was found to be both thermodynamically (ΔE = +0.71 eV) and kinetically (energy barrier, E_a = 4.02 eV) unfavourable, which indicates that NO will remain molecularly chemisorbed on the {100} surface even at high temperatures.

{111} surface. The strongest surface–NO interaction was found on the {111} surface, which is the least stable surface among the four surfaces investigated. The lowest energy structure was calculated to be the Fe_2–NO configuration with the N atom bridging between the adjacent Fe atoms as shown in Fig. 7c, releasing an adsorption energy of 3.213 eV, *i.e.*, ∼0.3 eV more favourable than the lowest energy structures on the {011} and {100} surfaces. The two Fe–N and N–O bond distances are calculated to be 1.795 Å, 1.791 Å, and 1.209 Å respectively. When adsorbed *via* the oxygen atom, also preferentially at the bridging Fe sites as shown in Fig. 7d, the adsorption energy is calculated to be −1.48 eV *i.e.*, 1.73 eV less stable than the most favoured Fe_2–NO structure. The adsorption of the NO molecule onto the {111} surface is characterized by significant charge transfer from the surface; NO draws 0.64 e^- and 0.45 e^- from the surface when adsorbed in the Fe_2–NO and Fe_2–ON configurations respectively. This effect causes an elongation of the N–O bonds as shown in Table 3 along with the stretching N–O vibrational frequencies. Further analysis of the bonding of NO on the {111} surface was obtained through an analysis of the electronic DOS of the lowest energy Fe_2–NO system, projected on orbitals of nitrogen and oxygen species and of the interacting surface Fe atoms (Fig. 8). Comparing the DOS of NO in the non-interacting state (Fig. 8a) to that of the adsorbed state (Fig. 8b) one can observe the disappearance of the NO-2π states at the Fermi level upon adsorption, which therefore suggests a strong interaction between the adsorbate and the substrate Fe d-orbitals *via* mixing of this orbital.

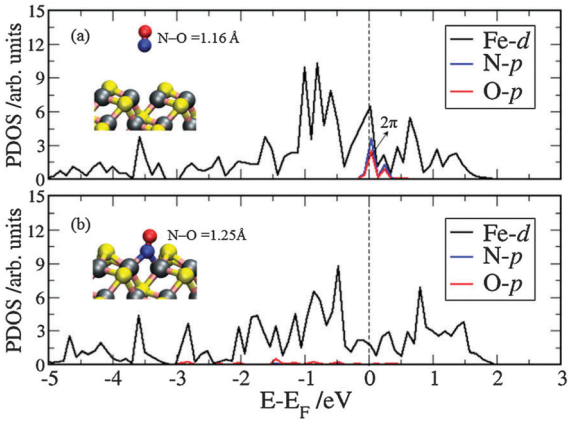

Fig. 8 Projected density of states (PDOS) for NO adsorbed onto FeS(111): (a) before interaction and (b) Fe_2–NO adsorption structure. The dashed line represents the Fermi level.

The minimum energy reaction pathway for NO dissociation on the {111} surface leaves the N and O adsorbed at bridge sites between two Fe atoms but, unlike on the {011} and {100} surfaces, the NO dissociation reaction on the {111} surface is exothermic ($\Delta E = -1.56$ eV) although the calculated high energy barrier of 3.96 eV suggests that this dissociation might occur only at high temperatures. The reaction profile for NO dissociation on the {011}, {100} and {111} surfaces is shown in Fig. 9.

3.4 NO_2 adsorption and dissociation

The optimized NO_2 adsorption structures with minimum energy on the {001}, {011}, {100} and {111} surfaces were calculated by considering four different initial adsorption configurations, *i.e.*, two bidentate configurations where the NO_2 binds either *via* two Fe–O bonds (denoted Fe–ONO–Fe) or *via* one Fe–O bond and the Fe–N bond (denoted Fe–NOO–Fe) and two monodentate configurations *via* a single Fe–N bond (Fe–NO_2) or a single Fe–O bond (Fe–ONO). We have also attempted to adsorb the NO_2 molecule at sulfur sites but found no stable chemisorbed S–NO_2 adsorption structure; the molecule always moves to a reactive Fe site during geometry optimization.

{001} surface. Similar to the weak interaction of NO with the {001} surface, we have also identified only a weak interaction between the NO_2 molecule and the {001} surface. The NO_2 molecule shows only physisorption on the surface and it moved away from the different surface binding sites during geometry optimizations from all initial orientations. The optimized NO_2 adsorption geometries on the {001} surface are shown in Fig. 10(a–c), while the adsorption energies and the relevant interatomic bond distances and angles are summarized in Table 4. The Fe–NOO–Fe, Fe–ONO–Fe, and Fe–ONO configurations released adsorption energies of 0.23 eV, 0.26 eV, and 0.17 eV, respectively, but when we attempted to adsorb the NO_2 at a sulfur site (*i.e.*, S–NO_2), it converged to the relaxed Fe–NOO–Fe structure. Consistent with physisorption, we observed no charge transfers between the {001} surface and the NO_2 molecule upon adsorption and the N–O bond distances remained relatively unaffected.

{011} surface. Compared to the {001} surface, the NO_2 molecule is chemisorbed strongly on the {011} surface. The optimized NO_2 adsorption structures on the {011} surface are shown in Fig. 11(a–c) and their corresponding iso-surfaces of the electron density difference are displayed in Fig. 11(d–f). The lowest energy structure is calculated to be the bidentate Fe–NOO–Fe structure (Fig. 11a), releasing an adsorption energy of 2.67 eV, with calculated Fe–N and Fe–O bond distances of 1.927 Å and 1.953 Å respectively. Bader population analysis indicates that the NO_2 molecule draws a charge of 0.78 e^- from the {011} surface upon adsorption which causes an elongation of the N–O bond distances calculated to be 1.349 Å and 1.229 Å, compared with the free unperturbed bond length of 1.213 Å. Consistent with the elongated N–O bonds, we observe a significant reduction in the N–O stretching frequencies of the adsorbed NO_2 molecule (Table 5) compared to the gas phase.

When the NO_2 molecule adsorbs *via* both oxygen atoms *i.e.*, the bidentate Fe–ONO–Fe configuration as shown in Fig. 11b, the adsorption energy is calculated to be −2.61 eV *i.e.*, only 0.05 eV less than in the most favourable Fe–NOO–Fe

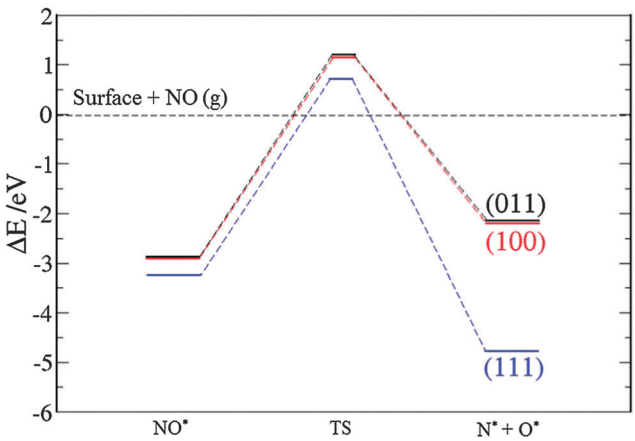

Fig. 9 Reaction profile for NO dissociation on the {011}, {100} and {111} FeS surfaces. The asterisks (*) denote the adsorbed species. The calculated (ΔE, E_a) are (+0.73 eV, 4.12 eV) on the {011} surface, (+0.71 eV, 4.02 eV) on the {100} surface and (−1.56 eV, 3.96 eV) on the {111} surface.

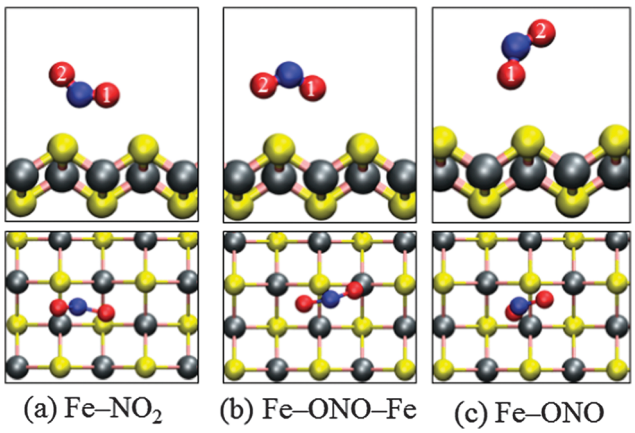

Fig. 10 Side and top views of the optimized adsorption structures of NO_2 on the {001} FeS surface. (Colour scheme: Fe = grey, S = yellow, N = blue and O = red).

Table 4 Adsorption energies and the relevant bond distances and angles of NO_2 adsorbed onto the {001}, {011}, {100} and {111} FeS surfaces. $\sum q$ denotes the net charge gained by the NO_2 molecule upon adsorption. The free N–O bond distance and the ∠O–N–O bond angel are calculated to be 1.213 Å and 133.8°, respectively, in excellent agreement with experimental[91] values of 1.197 Å and 134.1°

Surface	Configuration	E_{ads}/eV	d(Fe–N)/Å	d(Fe–O)/Å	d(N–O1)/Å	d(N–O2)/Å	∠ONO/°	$\sum q$/e$^-$
(001)	Fe–NOO–Fe	−0.23	3.707	3.853	1.224	1.221	130.7	0.00
	Fe–ONO–Fe	−0.26	—	3.827	1.226	1.226	131.5	0.00
	Fe–ONO	−0.17	—	3.901	1.225	1.218	131.3	0.00
(011)	Fe–NOO–Fe	−2.67	1.927	1.953	1.349	1.229	116.6	0.78
	Fe–ONO–Fe	−2.61	—	1.889	1.289	1.286	119.4	0.71
	Fe–ONO	−1.64	—	1.874	1.351	1.208	113.8	0.51
(100)	Fe–NOO–Fe	−2.73	1.924	1.950	1.362	1.228	116.7	0.80
	Fe–ONO–Fe	−2.64	—	1.857	1.294	1.292	119.3	0.78
	Fe–ONO	−1.65	—	1.825	1.415	1.201	111.9	0.52
(111)	Fe–NOO–Fe	−2.91	1.870	1.957	1.386	1.229	119.7	0.90
	Fe–ONO–Fe	−2.69	—	1.978	1.271	1.270	116.0	0.87
	Fe–ONO	−1.70	—	1.825	1.465	1.212	112.3	0.56

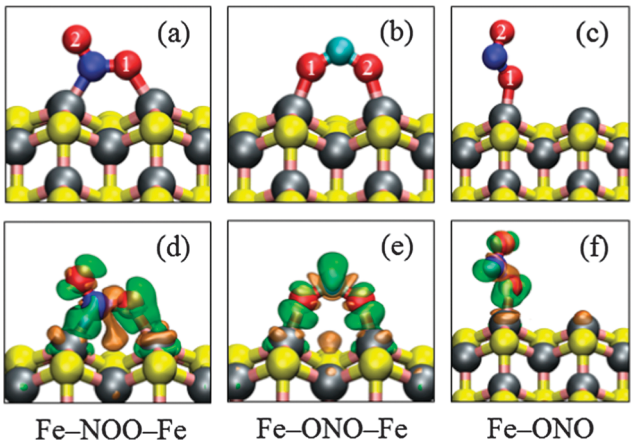

Fig. 11 Side views of the optimized adsorption structures of NO_2 (a–c) on the {011} FeS surface. The corresponding electron density difference plots relative to the adsorbed NO_2, showing charge transfer in the regions between NO_2 and the surface Fe atoms upon adsorption are displayed in (d–f). Green contours indicate electron density increase by 0.02 electrons per Å^3 and orange contours indicate electron density decrease by 0.02 electrons per Å^3. (Colour scheme: Fe = grey, S = yellow, N = blue and O = red).

structure. Bader population analysis indicates that a charge transfer of 0.71 e$^-$ occurs from the surface to the NO_2 molecule, which causes structural changes in the molecule; the ∠O–N–O bond angle reduces from 133.8° to 119.4° and the two N–O bond distances are calculated to be 1.289 Å and 1.286 Å, both suggesting an elongation of the N–O bonds relative to the free NO_2 molecule. The distances between the two oxygen atoms and the interacting surface Fe atoms (Fe–O) are 1.879 Å and 1.899 Å (the average value is reported in Table 4). The least stable configuration was calculated to be the monodentate oxygen (Fe–ONO) configuration (Fig. 11c), which releases an adsorption energy of 1.64 eV with an Fe–O bond distance of 1.874 Å. The smallest of charge transfers (0.51 e$^-$) from the surface occurred in this configuration and the N–O bonds are calculated to be 1.351 Å and 1.208 Å.

Table 5 The symmetric (υ_s), asymmetric (υ_{as}) and bending (υ_b) vibrational frequencies of NO_2 adsorbed onto the low-Miller index FeS surfaces

	System	υ_s/cm^{-1}	υ_{as}/cm^{-1}	υ_b/cm^{-1}
	NO_2 (g) Expt.[87]	1318	1610	750
	NO_2 (g) Calc.	1331	1665	730
(011)	Fe–NOO–Fe	845	1455	716
	Fe–ONO–Fe	1066	1088	713
	Fe–ONO	798	1594	611
(100)	Fe–NOO–Fe	847	1452	712
	Fe–ONO–Fe	1050	1064	724
	Fe–ONO	792	1591	604
(111)	Fe–NOO–Fe	839	1398	719
	Fe–ONO–Fe	1048	1052	727
	Fe–ONO	790	1588	612

An inspection of the iso-surfaces of NO_2 on the (011) surface in Fig. 11(d–f) shows significant charge redistribution within the NO_2–surface systems, which results in a net charge accumulation on the NO_2 molecule and in the bonding regions between NO_2 and the surface Fe atoms, which is consistent with the formation of chemical bonds. An inspection of the iso-surfaces reveals that some charge depletion occurs from Fe d-states and the adsorbed NO_2 molecule which suggests donation of electrons from the NO_2 into the empty Fe d-orbital and a back-donation from the filled Fe d-orbitals into the empty antibonding orbitals of NO_2. The calculated net charge accumulation on the adsorbed NO_2 molecule as estimated from our Bader population analysis indicates stronger back-donation from the interacting surface Fe d-orbitals to NO_2 compared to the forward donation from NO_2 to the surface.

The reaction profile for NO_2 dissociation on the {011} surface starting from the most stable bidentate Fe–NOO–Fe configuration is shown in Fig. 12. The dissociation proceeded in two steps: step 1 represents the cleavage of the first N–O bond to produce NO and O fragments adsorbed at the adjacent top-Fe sites (R1), and step 2 represents a further dissociation of the second N–O bond to produce either (N(ads) and O_2(ads)), R2-A or

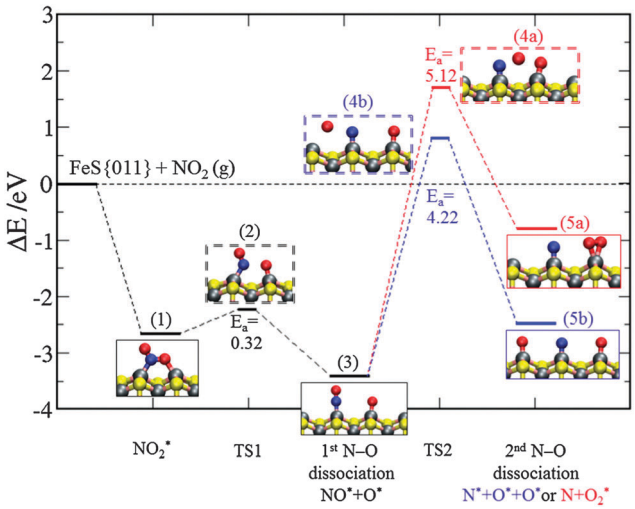

Fig. 12 Reaction profile for NO_2 dissociation on the FeS{011} surface. The insets show a schematic representation of the steady states, numbered in accordance with the relevant stage in the overall reaction. (Colour scheme: Fe = grey, S = yellow, N = blue and O = red). Note the transition states are framed in dashed lines and the asterisks (*) denote the adsorbed species.

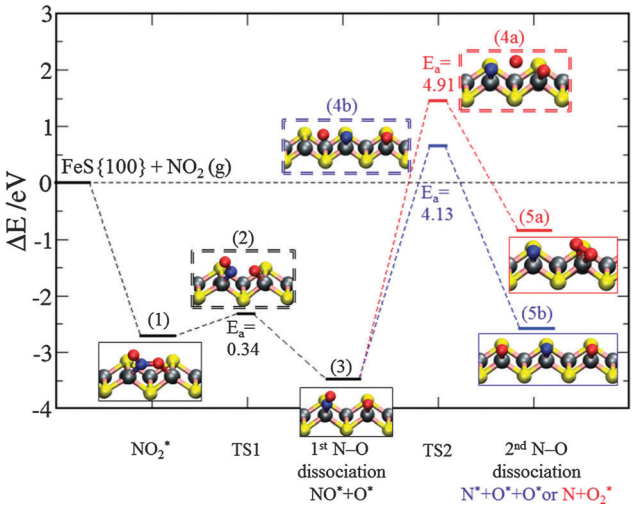

Fig. 14 Reaction profile for NO_2 dissociation on the FeS{100} surface. The insets show a schematic representation of the steady states, numbered in accordance with the relevant stage in the overall reaction. (Colour scheme: Fe = grey, S = yellow, N = blue and O = red). Note the transition states are framed in dashed lines and the asterisks (*) denote the adsorbed species.

adsorbed atomic species (*i.e.*, N(ads) and two O(ads)), R2-B. The cleavage of the first N–O bond (R1) was found to be exothermic (ΔE = −0.76 eV) and has a low activation energy barrier of 0.32 eV, which suggests that NO_2 will readily dissociate into NO(ads) and O(ads) species on the {011} surface. Further dissociation of the second N–O bond through reactions R2-A and R2-B is, however, both thermodynamically and kinetically unfavourable. Reactions R2-A and R2-B are, respectively, endothermic by 2.63 eV and 0.93 eV and have high activation energy barriers calculated to be 5.12 eV and 4.22 eV respectively, which suggests that complete dissociation of NO_2 on the {011} surface is unlikely to occur even at high temperatures.

{100} surface. The relaxed NO_2 adsorption structures on the {100} surface are shown in Fig. 13(a and b). As on the {011} surface, the lowest energy configuration was found to be a bidentate Fe–NOO–Fe (Fig. 13a), which releases an adsorption energy of 2.73 eV, *i.e.*, only 0.06 eV more favourable than the lowest energy structure on the {011} surface. Bader population analysis indicates that the NO_2 molecule draws 0.80 e^- from the surface which causes an elongation of the two N–O bonds (1.362 Å, 1.228 Å) and a reduction in the ∠O–N–O bond angle (133.8°→116.7°) as shown in Table 4. The other bidentate configuration with two Fe–O bonds (Fe–ONO–Fe), Fig. 13b is only 0.09 eV less favourable than the most stable bidentate Fe–NOO–Fe configuration, while the monodentate Fe–ONO configuration is up to 1.03 eV less favourable relative to the lowest energy bidentate Fe–NOO–Fe configuration. The close comparison between the binding energies of NO_2 on the {100} and {011} surfaces is in agreement with the small difference in their calculated surface energies; 1.04 J m^{-2} for (100) and 0.95 J m^{-2} for the (011) surface and suggest that both surfaces have similar reactivity toward NO_2 activation.

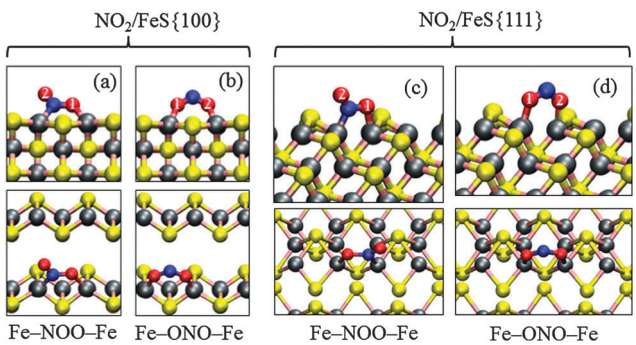

Fig. 13 Side (top) and top (bottom) views of the optimized adsorption structures of NO_2 on the {100}-(a, b) and {111}-(c, d) FeS surfaces. (Colour scheme: Fe = grey, S = yellow, N = blue and O = red).

The reaction profile for the dissociation of NO_2 from the most stable bidentate Fe–NOO–Fe configuration on the {100} surface is shown in Fig. 14. The dissociation of the first N–O bond produces NO and O that are adsorbed at the adjacent top-Fe sites and the reaction is exothermic (ΔE = −0.75 eV) with a low activation barrier of 0.30 eV, which is close to the barrier for the dissociation of the first N–O on the {011} surface (0.32 eV), and therefore suggests that NO_2 will also readily dissociate into NO(ads) and O(ads) fragments on the {100} surface. Again, as was found on the {011} surface, further dissociation of the second N–O bond to yield reaction R2-A or R2-B is found to be endothermic relative to the relaxed structure of the first N–O bond cleavage with high activation energy barriers. The (ΔE, E_a) for reactions R2-A and R2-B are (2.61, 4.91) and (0.89, 4.13), respectively, which again suggests that complete dissociation of NO_2 on the {100} surface is unlikely to occur even at high temperatures.

{111} surface. The strongest NO_2–FeS interaction was observed on the {111} surface, similar to the NO adsorption. The lowest energy structure (Fe–NOO–Fe), shown in Fig. 13c, released an

adsorption energy of 2.91 eV with the Fe–N and Fe–O bond distances calculated to be 1.870 Å and 1.957 Å. The highest charge transfer (0.90 e^-) between the FeS surface and NO_2 occurred in this configuration, which causes an elongation of the N–O bond distances calculated to be 1.386 Å and 1.229 Å, compared with the free unperturbed bond length of 1.213 Å. The ∠O–N–O bond angle is also reduced to 119.7° compared to the free NO_2 bond angle of 133.8°. The other bidentate configuration with two Fe–O bonds (Fe–ONO–Fe), Fig. 13d, released an adsorption energy of 2.69 eV, *i.e.*, 0.22 eV less favourable than the most stable Fe–NOO–Fe configuration. As was found on the {011} and {100} surfaces, the least stable adsorption structure on the {111} surface is calculated to be a monodentate Fe–O configuration (*i.e.*, Fe–ONO), which released an adsorption energy of 1.70 eV. Bader population analysis indicates that a charge transfer of 0.87 e^- and 0.56 e^- occurs from the surface to the NO_2 molecule when adsorbed in the bidentate Fe–ONO–Fe and monodentate Fe–ONO configurations respectively. This effect causes weakening of the N–O bonds as they are elongated relative to the free N–O bond distances (see Table 4).

To gain further insight into the strong interaction of NO_2 with the mackinawite surfaces, we have plotted the electronic DOS of the strongest surface–NO_2 system on the (111) surface, projected on orbitals of nitrogen and oxygen species and of the interacting surface Fe substrate. Before the adsorption of NO_2 (Fig. 15a), the projection on the N and O atoms and on the surface Fe atoms shows states at the Fermi level, which suggests that electron transfer can occur between the surface Fe atoms and the NO_2 molecule. Upon adsorption (Fig. 15b), the strong hybridization between the O and N p-orbitals and the surface Fe d-orbitals causes the abrupt disappearance of the molecule's states at the Fermi level, which is consistent with the strong interactions and significant calculated charge transfer. We also note a broadening of the N and O p-states at 1.0 eV upon adsorption, again suggesting their strong interaction with the surface Fe d-orbitals.

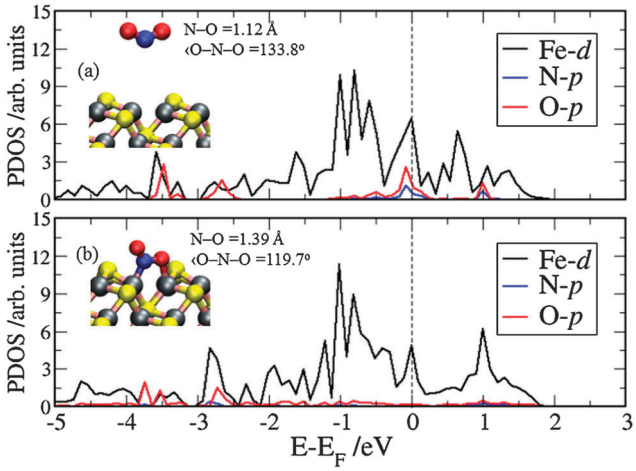

Fig. 15 Projected density of states (PDOS) for NO_2 adsorbed onto FeS{111}: (a) before interaction and (b) Fe–NOO–Fe adsorption structure. The dashed line represents the Fermi level.

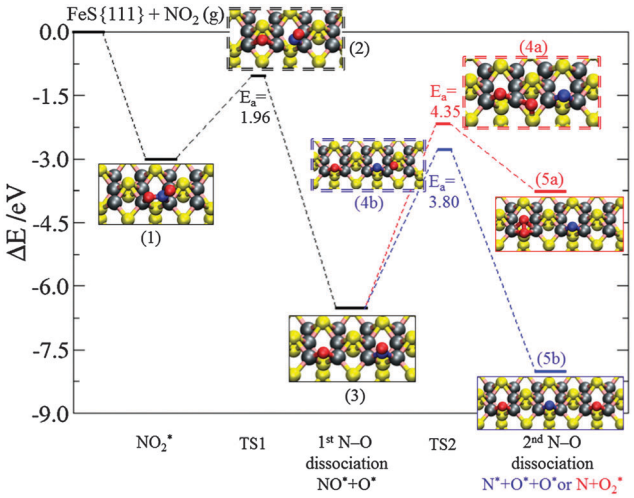

Fig. 16 Reaction profile for NO_2 dissociation on the FeS{111} surface. The insets show a schematic representation of the steady states, numbered in accordance with the relevant stage in the overall reaction. (Colour scheme: Fe = grey, S = yellow, N = blue and O = red). Note the transition states are framed in dashed lines and the asterisks (*) denote the adsorbed species.

The reaction profile for the dissociation of NO_2 from the most stable Fe–NOO–Fe configuration is shown in Fig. 16. The dissociation of the first N–O bond leaves the NO and O fragments adsorbed at bridge sites between two Fe atoms and the reaction is found to be highly exothermic (ΔE = −3.54 eV) but the total reaction barrier was calculated to be 1.96 eV. The higher activation barrier for the dissociation of the first N–O bond on the {111} surface compared to the {011} and {100} surfaces can be attributed to the additional energy required to move the dissociated products from the top-Fe site to the most stable bridging-Fe sites. The dissociation of the second N–O bond towards the production of N(ads) and two O(ads) was also found to be exothermic (ΔE = −1.45 eV) with an activation energy barrier of 3.80 eV, while the alternative path to produce N(ads) and O_2(ads) was found to be endothermic (ΔE = +2.78 eV) with a higher activation energy barrier of 4.35 eV. Although the thermodynamics favour the formation of N(ads) and two O(ads), the calculated high activation energy barrier suggests that this might only be attainable at higher temperatures. The unfavourable thermodynamics and kinetics for the production of N(ads) and O_2(ads), however, indicates that this reaction is unlikely to occur at all.

4. Summary and conclusions

From the geometry optimization of the low-Miller index surfaces of mackinawite, we have shown the {001} surface to be the most stable surface, followed by the {011}, {100}, {111} and {110} surfaces. Whereas the (001) surface is the most stable and therefore the dominant surface expressed in the morphology of the FeS crystal, our NO_x adsorption calculations show that it is the least reactive surface towards NO_x adsorption. The sides and corners of the mackinawite nanocrystal, which present the {011}, {100} and {111} surfaces, however, are shown to be very

reactive towards NO_x adsorption and activation. The strongest NO_x–FeS interaction was calculated on the (111) surface, the least stable surface among the surfaces investigated. The adsorption of the NO_x species onto the {011}, {100} and {111} surfaces was characterised by significant electron transfer from the interacting surface species, which causes weakening of the N–O bonds particularly the surface-bound N–O bond as it is elongated compared to the free unperturbed NO_2 bond length. Comparing the results obtained on the mackinawite surfaces to those obtained on the pyrite (100) surface,[49] we found that the NO_x species interact more strongly with mackinawite surfaces than the pyrite (100) surface, which indicates that mackinawite surfaces are more reactive towards NO_x adsorption and activation than the pyrite (100) surface. The stronger interaction of the NO_x species with the mackinawite surfaces compared to the pyrite (100) surface can be rationalized by considering the shorter Fe–N and Fe–O bond distances calculated on the mackinawite surfaces compared to the pyrite surfaces. Unlike the NO_x–pyrite interactions wherein the Fe–N bond distances for NO adsorption were reported to be 1.72–2.04 Å, the adsorption of NO onto the mackinawite surfaces yields shorter Fe–N bond distances, calculated to be 1.643–1.790 Å, which suggests stronger Fe–N bonds on the mackinawite surface than on the pyrite surface. Similarly, the shorter Fe–N (1.870–1.927 Å) and Fe–O (1.825–1.978 Å) bond distances calculated for the NO_2–mackinawite interactions compared to the slightly longer Fe–N (1.94 Å) and Fe–O (1.96–2.02 Å) bond distances in the NO_2–pyrite interactions suggest stronger binding of NO_2 to the mackinawite surfaces than to the pyrite surface.

Our calculated binding energies and interatomic Fe–N and Fe–O bond distances for the NO_x species on the mackinawite surfaces also compare well with those reported on the metallic Fe(111) surface.[89] Similar to the adsorption characteristics calculated on the mackinawite surfaces, adsorption of the NO_x species onto the Fe (111) surface was characterized by significant charge transfer from the interacting Fe atom with the NO_x species (0.72 to 1.19 e^- for NO_2), which gave rise to the stronger binding and larger distortion in the N–O bond distances observed.[89]

Our calculated reaction profiles for the dissociation of NO_2 show that the {011}, {100} and {111} surfaces exhibit considerable catalytic activity toward the cleavage of the first N–O bond to produce NO(ads) and O(ads) fragments, with favourable thermodynamics and kinetics. The calculated high activation energy barriers for the further dissociation of the second N–O bond to produce either (N(ads) and O_2(ads)) or (N(ads) and two O(ads)), however, suggest that a complete dissociation of NO_2 is not likely to occur on the {011} and {100} surfaces but could occur on the {111} mackinawite surface at high temperatures. This information about the reaction mechanism, the catalytic activity of the major surfaces, and the importance of the surface structure would otherwise be difficult to obtain with experimental measurements, indicating that periodic DFT calculations might play a vital role in the rational design of improved catalytic FeS surfaces for the adsorption and dissociation of environmentally important NO_x molecules.

Acknowledgements

N.Y.D. acknowledges University College London for an Overseas Research Scholarship and N.H.dL. acknowledges the UK Engineering and Physical Sciences Research Council (EPSRC) for funding (Grant No. EP/H046313/1). This work made use of the facilities of HECToR, the UK's national high-performance computing service *via* our membership of the UK's HPC Materials Chemistry Consortium, which is funded by the EPSRC (EP/F067496). The authors also acknowledge the use of the UCL@Legion High Performance Computing Facility, and associated support services, in completion of this work.

References

1 V. Schmatloch and N. Kruse, *Surf. Sci.*, 1992, **270**, 488.
2 W. A. Brown and D. A. King, *J. Phys. Chem. B*, 2000, **104**, 2578.
3 H. Tang and B. L. Trout, *J. Phys. Chem. B*, 2005, **109**, 17630.
4 S. C. Xu, S. Irle, D. G. Musaev and M. C. Lin, *J. Phys. Chem. B*, 2006, **110**, 21135.
5 A. Hellman, I. Panas and H. Grönbeck, *J. Chem. Phys.*, 2008, **128**, 104704.
6 M. Breedon, M. J. S. Spencer and I. Yarovsky, *Surf. Sci.*, 2009, **603**, 3389.
7 G. Liu and P.-X. Gao, *Catal. Sci. Technol.*, 2011, **1**, 552.
8 Z. M. Liu and S. I. Woo, *Catal. Rev.*, 2006, **48**, 43.
9 R. Burch, J. P. Breen and F. C. Meunier, *Appl. Catal., B*, 2002, **39**, 283.
10 J. A. Rodriguez, T. Jirsak, G. Liu, J. Hrbek, J. Dvorak and A. Maiti, *J. Am. Chem. Soc.*, 2001, **123**, 9597.
11 D. C. Sorescu, C. N. Rusu and J. T. Yates Jr., *J. Phys. Chem. B*, 2000, **104**, 4408.
12 M. M. Branda, C. D. Valentin and G. Pacchioni, *J. Phys. Chem. B*, 2004, **108**, 4752.
13 Z. Liu, L. Ma and A. S. M. Junaid, *J. Phys. Chem. C*, 2010, **114**, 10.
14 J. Segner, W. Vielhaber and G. Ertl, *Isr. J. Chem.*, 1982, **22**, 375.
15 D. Dahlgren and J. C. Hemminger, *Surf. Sci.*, 1982, **123**, 739.
16 M. E. Bartram, R. G. Windham and B. E. Koel, *Surf. Sci.*, 1987, **184**, 57.
17 M. E. Bartram, R. G. Windham and B. E. Koel, *Langmuir*, 1988, **4**, 240.
18 U. Schwalke, J. E. Parmeter and W. H. Weinberg, *J. Chem. Phys.*, 1986, **84**, 4036.
19 U. Schwalke, J. E. Parmeter and W. H. Weinberg, *Surf. Sci.*, 1986, **178**, 625.
20 T. Jirsak, J. Dvorak and J. A. Rodriguez, *Surf. Sci.*, 1999, **436**, L683.
21 S. R. Bare, K. Griffiths, W. N. Lennard and H. T. Tang, *Surf. Sci.*, 1995, **342**, 185.
22 G. Polzonetti, P. Alnot and C. R. Brundle, *Surf. Sci.*, 1990, **238**, 226.
23 G. Polzonetti, P. Alnot and C. R. Brundle, *Surf. Sci.*, 1990, **238**, 237.
24 W. A. Brown, P. Gardner and D. A. King, *Surf. Sci.*, 1995, **330**, 41.

25 B. A. Banse and B. E. Koel, *Surf. Sci.*, 1990, **232**, 275.
26 D. T. Wickham, B. A. Banse and B. E. Koel, *Surf. Sci.*, 1991, **243**, 83.
27 M. E. Bartram and B. E. Koel, *Surf. Sci.*, 1989, **213**, 137.
28 J. Wang and B. E. Koel, *J. Phys. Chem. A*, 1998, **102**, 8573.
29 J. Wang, M. R. Voss, H. Busse and B. E. Koel, *J. Phys. Chem. B*, 1998, **102**, 4693.
30 M. Beckendorf, U. J. Katter, H. Schlienz and H. J. Freund, *J. Phys. Chem.*, 1993, **5**, 5471.
31 D. T. Wickham, B. A. Banse and B. E. Koel, *Catal. Lett.*, 1990, **6**, 163.
32 B. Geng, X. Liu, J. Ma and Q. Du, *Mater. Sci. Eng., B*, 2007, **145**, 17.
33 M. Akhtar, J. Akhter, M. A. Malik, P. O'Brien, F. Tuna, J. Raftery and M. Helliwell, *J. Mater. Chem.*, 2011, **21**, 9737.
34 A. L. Abdelhady, M. A. Malik, P. O'Brien and F. Tuna, *J. Phys. Chem. C*, 2012, **116**, 2253.
35 J. Joo, H. B. Na, T. Yu, J. H. Yu, Y. W. Kim, F. Wu, J. Z. Zhang and T. Hyeon, *J. Am. Chem. Soc.*, 2003, **125**, 11100.
36 A. Ennaoui, S. Fiechter, W. Jaegermann and H. Tributsch, *J. Electrochem. Soc.*, 1986, **133**, 97.
37 G. Chen, J. M. Zen, F. R. Fan and A. J. Bard, *J. Phys. Chem.*, 1991, **95**, 3682.
38 N. Y. Dzade, A. Roldan and N. H. de Leeuw, *J. Chem. Phys.*, 2013, **139**, 124708.
39 A. J. Devey, R. Grau-Crespo and N. H. de Leeuw, *J. Phys. Chem. C*, 2008, **112**, 10960.
40 S. Haider, A. Roldan and N. H. de Leeuw, *J. Phys. Chem. C*, 2014, **118**, 1958.
41 G. Wächtershäuser, *Prog. Biophys. Mol. Biol.*, 1992, **58**, 85.
42 E. Blöchl, M. Keller, G. Wächtershäuser and K. O. Stetter, *Proc. Natl. Acad. Sci. U. S. A.*, 1992, **89**, 8117.
43 G. D. Cody, N. Z. Boctor, T. R. Filley, R. M. Hazen, J. H. Scott, A. Sharma and H. S. Yoder Jr., *Science*, 2000, **289**, 1337.
44 P. G. Moses, J. J. Mortensen, B. I. Lundqvist and J. K. Nørskov, *J. Chem. Phys.*, 2009, **130**, 104709.
45 B. Hinnemann, P. G. Moses, J. Bonde, K. P. Jorgensen, J. H. Nielsen, S. Horch, I. Chorkendorff and J. K. Norskov, *J. Am. Chem. Soc.*, 2005, **127**, 5308.
46 P. G. Moses, B. Hinnemann, H. Topsøe and J. K. Nørskov, *J. Catal.*, 2007, **248**, 188.
47 J. V. Lauritse, J. Kibsgaard, G. H. Olesen, P. G. Moses, B. Hinnemann, S. Helveg, J. K. Nørskov, B. S. Clausenc, H. Topsøe and E. L. F. Besenbacher, *J. Catal.*, 2007, **249**, 220.
48 S. Cristol, J. Paul, C. Schovsbo, E. Veilly and E. Payen, *J. Catal.*, 2006, **239**, 145.
49 M. Sacchi, M. C. E. Galbraith and S. J. Jenkins, *Phys. Chem. Chem. Phys.*, 2012, **14**, 3627.
50 D. Rickard and G. W. Luther, *Chem. Rev.*, 2007, **107**, 514.
51 A. R. Lennie, S. A. T. Redfern, P. E. Champness, C. P. Stoddart, P. F. Schofield and D. J. Vaughan, *Am. Mineral.*, 1997, **82**, 302.
52 J. H. P. Watson, B. A. Cressey, A. P. Roberts, D. C. Ellwood, J. M. Charnock and A. K. Soper, *J. Magn. Magn. Mater.*, 2000, **214**, 13.
53 M. Wolthers, L. Charlet, C. H. van Der Weijden, P. R. van der Linde and D. Rickard, *Geochim. Cosmochim. Acta*, 2005, **69**, 3483.
54 A. C. Scheinost and L. Charlet, *Environ. Sci. Technol.*, 2008, **42**, 1984.
55 F. R. Livens, M. J. Jones, A. J. Hynes, J. M. Charnock, J. F. Mosselmans, C. Hennig, H. Steele, D. Collison, D. J. Vaughan, R. A. Pattrick, W. A. Reed and L. N. Moyes, *J. Environ. Radioact.*, 2004, **74**, 211.
56 M. Mullet, S. Boursiquot and J. J. Ehrhardt, *Colloids Surf., A*, 2004, **244**, 77.
57 A. R. Lennie, S. A. T. Redfern, P. F. Schofield and D. J. Vaughan, *Mineral. Mag.*, 1995, **59**, 677.
58 R. A. Berner, *Science*, 1962, **137**, 669.
59 E. F. Bertaut, P. Burlet and J. Chappert, *Solid State Commun.*, 1965, **3**, 335–338.
60 D. J. Vaughan and M. S. Ridout, *J. Inorg. Nucl. Chem.*, 1971, **33**, 741.
61 A. Subedi, L. J. Zhang, D. J. Singh and M. H. Du, *Phys. Rev. B: Condens. Matter Mater. Phys.*, 2008, **78**, 134514.
62 L. Ehm, F. M. Michel, S. M. Antao, C. D. Martin, P. L. Lee, m. S. D. Shastri, P. J. Chupas and J. B. Parise, *J. Appl. Crystallogr.*, 2009, **42**, 15.
63 S. Boursiquot, M. Mullet, M. Abdelmoula, J.-M. Génin and J.-J. Ehrhardt, *Phys. Chem. Miner.*, 2001, **28**, 600.
64 G. Kresse and J. Furthmuller, *Comput. Mater. Sci.*, 1996, **6**, 15.
65 G. Kresse and J. Furthmuller, *Phys. Rev. B: Condens. Matter Mater. Phys.*, 1996, **54**, 11169.
66 G. Kresse and J. Hafner, *Phys. Rev. B: Condens. Matter Mater. Phys.*, 1993, **48**, 13115.
67 G. Kresse and J. Hafner, *J. Phys.: Condens. Matter*, 1994, **6**, 8245.
68 S. Grimme, *J. Comput. Chem.*, 2006, **27**, 1787.
69 J. P. Perdew and A. Zunger, *Phys. Rev. B: Condens. Matter Mater. Phys.*, 1981, **23**, 5048.
70 J. P. Perdew, J. A. Chevary, S. H. Vosko, K. A. Jackson, M. R. Pederson, D. J. Singh and C. Fiolhais, *Phys. Rev. B: Condens. Matter Mater. Phys.*, 1992, **46**, 6671.
71 P. E. Blochl, *Phys. Rev. B: Condens. Matter Mater. Phys.*, 1994, **50**, 17953.
72 G. Kresse and D. Joubert, *Phys. Rev. B: Condens. Matter Mater. Phys.*, 1999, **59**, 1758.
73 G. W. Watson, E. T. Kelsey, N. H. de Leeuw, D. J. Harris and S. C. Parker, *J. Chem. Soc., Faraday Trans.*, 1996, **92**, 433.
74 P. W. Tasker, *J. Phys. C: Solid State Phys.*, 1979, **12**, 4977.
75 R. F. W. Bader, *Atoms in Molecules: A Quantum Theory*, Oxford University Press, London, 1994.
76 G. Henkelman, A. Arnaldsson and H. Jonsson, *Comput. Mater. Sci.*, 2006, **36**, 354.
77 G. Mills, H. Jónsson and G. K. Schenter, *Surf. Sci.*, 1995, **324**, 305.
78 A. Ulitsky and R. Elber, *J. Chem. Phys.*, 1990, **92**, 1510.
79 D. J. Vaughan and J. R. Craig, *Mineral Chemistry of Metal Sulfides*, Cambridge University Press, New York, 1978.
80 A. Hung, I. Yarovsky, J. Muscat, S. Russo, I. Snook and R. O. Watts, *Surf. Sci.*, 2002, **501**, 261.
81 H. Y. Jeong, J. H. Lee and K. F. Hayes, *Geochim. Cosmochim. Acta*, 2008, **72**, 493.

82 M. Wolthers, S. J. van der Gaast and D. Rickard, *Am. Mineral.*, 2003, **88**, 2007.
83 G. Wulff, *Z. Kristallogr., Kristallgeom., Kristallphys., Kristallchem.*, 1901, **39**, 449.
84 H. Ohfuji and D. Rickard, *Earth Planet. Sci. Lett.*, 2006, **241**, 227.
85 R. Burch, S. T. Daniells and P. Hu, *J. Chem. Phys.*, 2002, **117**, 2902.
86 M. Gajdoš, J. Hafner and A. Eichler, *J. Phys.: Condens. Matter*, 2006, **18**, 41.
87 L.-Y. Gan, R.-Y. Tian, X.-B. Yang, S.-L. Peng and Y.-J. Zhao, *Phys. Chem. Chem. Phys.*, 2011, **13**, 14466.
88 G. Blyholder, *J. Phys. Chem.*, 1964, **68**, 2772.
89 H. L. Chen, S. Y. Wu, H. T. Chen, J. G. Chang, S. P. Ju, C. Tsai and L. C. Hsu, *Langmuir*, 2010, **26**, 7157.
90 K. Nakamoto, *Infrared and Raman Spectra of Inorganic and Coordination Compounds*, Wiley, New York, 1997.
91 D. R. Lide, *Physical Constants of Organic Compounds, CRC Handbook of Chemistry and Physics*, Taylor and Francis, Boca Raton, FL, 2007.

